Solar Atmosphere Wave Dynamics Generated by Solar Global Oscillating Eigenmodes

M. K. Griffiths[1,]

Solar Physics and Space Plasma Research Centre (SP²RC), School of Mathematics and Statistics, University of Sheffield, Hicks Building, Hounsfield Road, S7 3RH, UK

V. Fedun

Department of Automatic Control and Systems Engineering, The University of Sheffield, Mappin Street, Sheffield, S1 3JD, UK

R. Erdélyi

Solar Physics and Space Plasma Research Centre (SP²RC), School of Mathematics and Statistics, University of Sheffield, Hicks Building, Hounsfield Road, S7 3RH, UK

Abstract

The solar atmosphere exhibits a diverse range of wave phenomena one of the earliest to be discovered was the five minute oscillation, the p-mode. The analysis of wave propagation in the solar atmosphere may be used as a diagnostic tool to measure the physical characteristics of the suns atmospheric layers.

In this paper we investigated the dynamics and propagation of waves which are generated by the solar global eigenmodes. We report on a series of hydrodynamic simulations of a realistic model of the solar atmosphere. With the objective of recreating atmospheric motions generated by global resonant oscillation the simulations use a driver which is spatially structured and extended in a sinusoidal profile across the computational model. The drivers perturb the region at 0.5 Mm above the bottom boundary of the

Email addresses: m.griffiths@sheffield.ac.uk (M. K. Griffiths), v.fedun@sheffield.ac.uk (V. Fedun), r.von.fay-siebenburgen@sheffield.ac.uk (R. Erdélyi)

[1]Corporate Information and Computing Services, The University of Sheffield, 10-12 Brunswick Street, Sheffield, S10 2FN, UK.

model and coincident with the temperature minimum. A combination of the VALIIIC and McWhirter solar atmospheres and coronal density profiles were used as the background equilibrium model in the simulations. We report on a study of synthetic photospheric oscillations for a magnetic field free model of the quiet Sun. To carry out the simulations, we employed the Magnetohydrodynamics code, SMAUG (Sheffield MHD Accelerated Using GPUs).

Our results show that the amount of energy propagated into the solar atmosphere is consistent with a model of solar global oscillations described using the Klein-Gordon equation. The calculated results indicate a power law consistent with observational results obtained using Solar Dynamics Observatory Atmospheric Imaging Assembly Ireland et al. (2015).

Keywords: magnetohydrodynamics (MHD); oscillations; MHD waves; solar atmosphere

1. Introduction

The highly magnetised solar atmosphere exhibits a diverse range of wave phenomena. Using solar observations in the Ca K band Leighton (1960) reported the first observations of oscillatory behaviour with vertical motions on the solar surface, an amplitude of 300-400 m/s and a period of 296 s. These ubiquitous oscillations are referred to as the p-modes these standing acoustic waves in the solar interior were explained by Ulrich (1970). Leibacher and Stein (1971) reported analysis indicating that the vertical wavelength is comparable to the horizontal wavelength and is 1-5 Mm. The main restoring force for these modes of oscillation is the pressure, the 5 minute oscillation is the main manifestation of these modes. The solar p-modes are generated by global resonant oscillations, periodic and turbulent motions just beneath the photosphere. These resonant modes are reflected at the surface by the steep change in density. The increase of the sound speed causes refraction. The resulting propagation of this wave energy into the solar atmosphere may be used as a diagnostic tool to understand the physical characteristics of the solar atmospheric layers. The detection of oscillations in the apparent solar diameter (see e.g Hill, 1976; Brown et al., 1978) was one of the first suggestions of the truly global oscillations of the sun. Wave propagation in a medium such as the gravitationally stratified solar atmosphere results in the occurrence of eigen-oscillations, these oscillations result from the inter-

nal interactions of the system. A model for understanding these oscillations can be understood from the normal mode solutions of the gravitating hydrodynamic slab in ideal MHD Goedbloed and Poedts (2004). The work of Christensen-Dalsgaard modelling solar oscillations on the basis of the solar structure provided spectra consistent with those of Hill (1976); Brown et al. (1978), this was the start of helioseismology. We report on a series of hydrodynamical simulations modelling a realistic temperature, pressure and density solar atmosphere using a driver located at the temperature minimum mimicking the the various p-modes. The driver is extended in a sinusoidal profile across the base of the computational model. The objectives of this work is to recreate the atmospheric motions generated by the global resonant oscillation, to understand how the energy provided by different modes of oscillation are redistributed in the solar atmosphere and to shed light on the mechanisms which lead to ubiquitous intensity oscillations in the solar atmosphere.

There is a significant number of works reporting on observational, theoretical and computational studies of p-mode phenomena. Observational and theoretical analysis generally describes mechanisms for the propagation of energy into the chromosphere, into the solar corona or between the transition region and the corona. We briefly summarise some of this work here. The growing field of coronal seismology uses the observed solar atmospheric wave modes to determine the physical characteristics of the solar atmosphere. This in turn requires a thorough understanding of the physics of the solar atmosphere. Although there is overwhelming evidence for photospheric 5 minute p-modes and 3 minute chromospheric modes, the detection and characterisation of oscillatory phenomena in the corona are rare and difficult to identify. This makes the solution of the coronal heating problem more challenging. However, since the advent of coronal seismology (see e.g Roberts et al., 1984; De Moortel, 2005) many spaced based high resolution solar observations e.g. SOHO, TRACE and SDO (to name but a few) have provided evidence for wave phenomena in the solar atmosphere.

Using SDO/AIA data Erdélyi et al. (submitted 2017) study image sequences at solar minimum and maximum for different solar regions e.g. active regions, quiet sun and a coronal hole. The authors consider a lower coronal channel, hot coronal channel and a cooler coronal channel. The study revealed strong 3-5 minute oscillations in all channels and included some longer period modes. The results indicated that differences my arise when the size of the area of observation is changed.The ubiquity of the ob-

served 3 and 5 minute oscillations in all channels and regions is an indication of a global excitation mechanism.

Imagery from SDO 171$\mathring{A}$ and 193$\mathring{A}$ was used by Ireland et al. (2015) to compute the Fourier power spectra in the solar corona. By analysing wave propagation in four regions of the solar atmosphere with different characteristics, they found that the distribution obeys a power law at low frequencies and possesses a flat distribution at high frequencies. This contrasts with the idea of a Gaussian noise distribution and a long time scale background. The implication is that this is the result of solar atmospheric heating from everywhere by small energy deposition events. It is expected that further measurements will constrain computational models.

Evidence for the upward propagation of acoustic wave with increasing amplitude has been demonstrated through a studies of variation in the intensities of chromospheric lines for example the Ca lines at 854 nm (see Beck et al. (2012)). Although the observed variations are unlikely to provide temperature rises observed in the chromosphere they are a clear indication of the increase in dynamical activity from the photosphere to the chromosphere. The analysis of observations by Bello González et al. (2009) find that at a height of 250 km there is an acoustic energy flux of 3000 W/m^2 2/3 of this energy is propagated by waves in the frequency range 5-10 mHz, the remaining third is carried by waves in the frequency range 10-20mHz. Waves with frequencies greater than the acoustic cut-off of 190s can contribute to the heating of the solar chromosphere. Reporting on measurements from the the Fe I 5434 $\mathring{A}$ Bello González et al. (2010) detect waves with periods down to 40 s. For periods below the cut-off of 190 s 40% of wave detections are above granules the remaining 60% are above the intergranules. The reported best estimate of the energy flux above granules is around 3000 W/m^2 whilst above the intergranules it is around 955 W/m^2. Most of the acoustic flux is found between 110s and 193s.

Using the IMAX instrument on the sunrise observatory, Roth et al. (2010) reported evidence for the excitation of solar acoustic oscillations excited by turbulent flows in the dark intergranular lanes. Individual sunquakes with epicentres near the solar surface and located in the intergranular lanes, are assumed to feed continuously energy into the resonant p-modes of the Sun and provide sources for acoustic oscillations. Roth et al. (2010) presents wavefronts rippling near a granule and oriented along the direction of the intergranular lane. Using simultaneous observations of the Na and K lines with Doppler measurements Jefferies et al. (2006) shows that inclined mag-

netic field lines provide portals along which magneto-acoustic energy can propagate at the intergranular boundaries.

There is a large body of computational work already undertaken to understand the propagation of waves in the solar atmosphere.Fedun et al. (2009) studied the oscillatory response of the 3D solar atmosphere to the leakage of photospheric motion results are discussed in detail. High-frequency waves are shown to propagate from the lower atmosphere across the transition region, experiencing relatively low reflection, and transmitting most of their energy into the corona. It is also observed that the thin transition region becomes a wave guide for horizontally propagating surface waves for a wide range of driver periods, and particularly at those periods that support chromospheric standing waves. Additionally, the magnetic field acts as a waveguide for both high- and low-frequency waves originating from the photosphere and propagating through the transition region into the solar corona. Previous work has considered either point source drivers with a gaussian velocity distribution. Other work e.g. Murawski and Zaqarashvili (2010) has demonstrated that a strong initial pulse may lead to the quasi periodic rising of chromospheric material into the lower corona in the form of spicules Khomenko and Calvo Santamaria (2013). Kalkofen et al. (2010) considered the propagation of acoustic modes in a stratified hydrodynamical model of the solar atmosphere, they employed a cylindrically symmetric driver with a diameter of approximately 1 Mm. They conclude that for driving regions of sizes smaller than the atmospheric scale height they are able to reproduce expansion waves which are characteristic of chromospheric bright points. With a weak horizontal magnetic field, the physics within the interior of supergranulation cells Lites et al. (2008) is suitably simple for undertaking hydrodynamic modelling. The modes modelled in this paper are mimicking global eigenmodes, the coherence length of eigenoscillations at the photosphere is 4 Mm, and the power peaks at 5 mins.

2. Numerical Computation Methods

The 3D numerical simulations described here were undertaken using Sheffield MHD Accelerated Using GPUs (SMAUG, Griffiths et al., 2015), the GPU implementation of the Sheffield Advanced Code (SAC, Shelyag et al., 2008). SAC and SMAUG are numerical MHD solvers allowing us to model the time-dependent evolution of photospheric oscillations in the solar atmosphere. SAC is a derivative of the versatile advection code (VAC) developed by

(Tóth, 1996). With the upper boundary of our model in the solar corona and the lower boundary in the photosphere the SMAUG code is well suited for modelling the leakage of wave energy from the photosphere, through the transition region and into the corona. We used open boundary conditions for the lower and upper boundaries which allowed us to model wave propagation for time scales characterised by the 5 minute p-mode induced oscillations. The general system of MHD equations are

$$\frac{\partial \rho}{\partial t} + \nabla \cdot (\mathbf{v}\rho) = 0, \tag{1}$$

$$\frac{\partial (\rho \mathbf{v})}{\partial t} + \nabla \cdot (\mathbf{v}\rho\mathbf{v} - \mathbf{B}\mathbf{B}) + \nabla p_t = \rho \mathbf{g}, \tag{2}$$

$$\frac{\partial e}{\partial t} + \nabla . (\mathbf{v}e - \mathbf{B}\mathbf{B} \cdot \mathbf{v} + \mathbf{v}p_t) + \nabla p_t = \rho \mathbf{g} \cdot \mathbf{v}, \tag{3}$$

$$\frac{\partial \mathbf{B}}{\partial t} + \nabla \cdot (\mathbf{v}\mathbf{B} - \mathbf{B}\mathbf{v}) = 0. \tag{4}$$

Here, ρ is the mass density, $\mathbf{v}$ is the velocity, $\mathbf{B}$ is the magnetic field, e is the energy density, p_t is the total pressure and $\mathbf{g}$ is the gravitational acceleration vector. The total pressure p_t is written as

$$p_t = p_k + \frac{\mathbf{B}^2}{2}, \tag{5}$$

where p_k is the kinetic pressure given by

$$p_k = (\gamma - 1)(e - \frac{\rho \mathbf{v}^2}{2} - \frac{\mathbf{B}^2}{2}). \tag{6}$$

Equations (1) to (6) are applicable to an ideal compressible plasma. The SAC code is based on perturbed versions of these equations, thus the variables ρ, e and $\mathbf{B}$ are expressed in terms of perturbed and background quantities as

$$\rho = \tilde{\rho} + \rho_b, \tag{7}$$

$$e = \tilde{e} + e_b, \tag{8}$$

$$\mathbf{B} = \tilde{\mathbf{B}} + \mathbf{B}_b. \tag{9}$$

where $\tilde{\rho}$ is the perturbed density, $\tilde{e}$ is the perturbed energy and $\tilde{\mathbf{B}}$ is the perturbed magnetic field. The background quantities with a subscript b do not change in time, as we assume a magneto-hydrostatic equilibrium of the background plasma which may have a gravitational field present, denoted by $\mathbf{g}$. Hyper-diffusion and hyper-resistivity are implemented to achieve numerical stability of the computed solution of the MHD equations (see for example Caunt and Korpi, 2001). The full set of MHD equations, including the hyper-diffusion source terms are given in Griffiths et al. (2015) and Shelyag et al. (2008).

3. Solar Atmospheric Model

To simulate oscillatory phenomena in the solar corona a physically representative model of the solar atmosphere is needed. An option is the use of a parametrisation of the temperature of the solar atmosphere which may be a smoothed step function profile Murawski and Zaqarashvili (2010). Results have demonstrated the need for observationally derived semi-empirical models of the solar atmosphere. There is much discussion about model validity and the work undertaken to demonstrate the reliability of the assumptions used to construct realistic models of the solar chromosphere Carlsson and Stein (1995), Kalkofen (2012). The contention arises from the dynamical nature of the solar chromosphere for example local dynamo action has been suggested as a mechanism of Joule heating in the solar chromosphere Leenaarts et al. (2011). The model atmosphere employed here is an observationally derived semi-empirical representation of the quiet sun. With the fundamental assumption of hydrostatic equilibrium a model of the chromosphere in equilibrium is constructed using the VALIIIc model, see Vernazza et al. (1981). For the region of the solar atmosphere above 2.5 Mm the results of the energy balance model of solar coronal heating has been used (see McWhirter et al., 1975), his model includes an acoustic contribution comparable to the hydrostatic pressure. The corresponding temperature and density profiles are shown in Figure (1).

4. Numerical Drivers for *p*-mode Oscillations

For this study the model requires a driver mimicing the solar global oscillations. The overview of observational studies identified a range of physical phenomena resulting in oscillatory behaviour and delivering energy into the

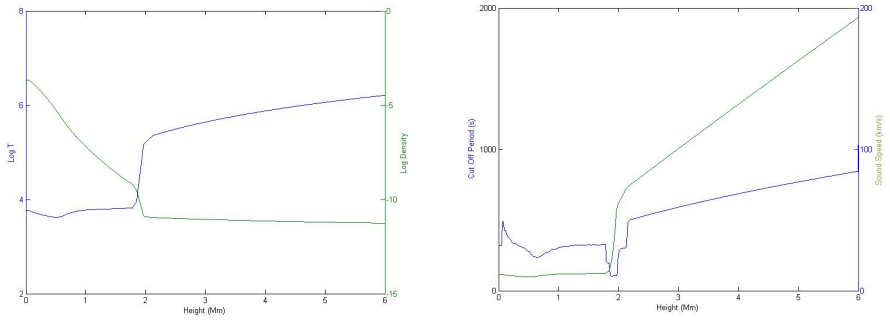

Figure 1: Temperature and density profiles (left) used for the model atmosphere and cut-off frequency at different heights (right).

solar atmosphere. The results presented here extend earlier work undertaken by Malins (2007), for their study point drivers were used to represent periodic buffeting or turbulent motions in the photosphere. The point driver is described by Equation (10)

$$V_z = A \sin\left(\frac{2\pi t}{T_s}\right) \exp\left(\frac{-(x-x_0)^2}{\Delta x^2}\right) \exp\left(\frac{-(z-z_0)^2}{\Delta z^2}\right). \qquad (10)$$

Here Δx and Δz are driver width in x and z directions correspondingly. In our 2D model we choose $\Delta x = 4$ Mm and $\Delta z = 4$ km. The results of the study demonstrated surface wave phenomena and structures in the transition region and highlighted the characteristics of the oscillatory phenomena as a result of frequency cut-offs induced by the stratified solar atmosphere. In contrast to the earlier models, the whole boundary of the model was perturbed. In the real Sun, photospheric p-mode oscillations have a horizontal wavelength and coherence. Here, these excitations are represented with a vertical velocity driver located at the photosphere, his acoustic p-mode driver excites waves which propagate into a realistic 3D model of the solar atmosphere. Drivers representing different modes are considered, for example an extended driver with a sinusoidal dependence and a wavelength of 8 Mm applied along the middle of the base of a computational domain of dimension 4 Mm represents a *fundamental mode*. A driver with wavelength 4 Mm applied the same way represents the *first harmonic* a *second harmonic* with wavelength 2 Mm was also considered. Drivers may be constructed as an ensemble of these solar global eigenmodes. The vertical location of this

extended driver is the temperature minimum which is 0.5 Mm above the lower boundary of the model i.e. the photosphere. Such a driver may be represented by an Equation (11) such as

$$V_z = A_{nm} \sin\left(\frac{2\pi t}{T_s}\right) \sin\left(\frac{(n+1)\pi x}{L_x}\right) \sin\left(\frac{(m+1)\pi y}{L_y}\right) \exp\left(\frac{-(z-z_0)^2}{\Delta z^2}\right), \tag{11}$$

where the mode is defined by the index n and m in Equations (10) and (11). Since we are investigating the leakage of energy into the solar atmosphere, for consistency it is necessary to ensure that for the different modes the driver amplitude is set to a value which provides the same total amount of energy over the model cross section and per unit time. For the n, m mode the energy, E_{nm} as a function of z and time may be written as;

$$E_{nm}(z,t) = \rho A_{nm}^2 I_{nm} \sin\left(\frac{2\pi t}{T_s}\right)^2 \exp\left(\frac{-(z-z_0)^2}{\Delta z^2}\right)^2, \tag{12}$$

where I_{nm} is

$$I_{nm} = \int_{-L_x}^{L_x} \int_{L_y}^{+L_y} \sin\left(\frac{(n+1)\pi x}{L_x}\right)^2 \sin\left(\frac{(m+1)\pi y}{L_y}\right)^2. \tag{13}$$

It is necessary to determine the amplitude A_{mn} for the different modes n, m with driver period T_s. This is achieved by computing the membrane energy integrated over the surface area and over a period of time from $t = 0$ to $t = T_m$ where T_m will correspond to the period of the driver with the largest value for the period. Following Leighton (1960), for the fundamental mode with driver period 300 s, we set A_{00}=350 ms^{-1}. Using Equation (12) to derive the ratio of the membrane energy for the mode n, m with driver period T_s, the mode $(0, 0)$ with driver period T_{00} and making $L_x = L_y$ gives the relation

$$A_{nm}^2 = \frac{2A_{00}^2}{(n^2 + m^2 + 2(n+m) + 2)} T_{rat}, \tag{14}$$

where T_{rat} is

$$T_{rat} = \frac{T_m - \frac{T_{00}}{4\pi} \sin(\frac{4\pi T_m}{T_{00}})}{T_m - \frac{T_s}{4\pi} \sin(\frac{4\pi T_m}{T_s})}. \tag{15}$$

This relation was used to determine the amplitudes for the higher order modes, starting from the A_{00} mode we used $A_{00} = 350\, ms^{-1}$.

set	description
a	Modes for the 30 s, 180 s and 300 s driver.
b	Normal Modes corresponding to different values of c_s
c	Normal Modes for equal mode values (i.e. $n = m$)

Table 1: Sets of simulations used to characterise oscillatory motions arising from an extended photospheric driver.

5. Numerical Analysis

Hydrodynamic simulations have been undertaken for a selection of drivers covering a range of time periods, modes and amplitudes supplying the same amount of energy, see Equation (12). For this investigation we have been guided by the requirement that different driver modes deliver the same total amount of energy over the model cross section and when integrated over a time interval corresponding to the period of the longest period driver used for the set of simulations. Three sets of simulations have been considered. Set (a) are the drivers selected because of their period, Set (b) are series of normal modes and Set (c) are normal modes with equal mode numbers (see Table (5)). The amplitudes for each of the modes are determined by using Equation (14). To use this relation, we assume that the $(0, 0)$ for the 300 s driver has an amplitude of 350 m/s (see Leighton, 1960).

The driver periods for set (a) correspond to the dominant atmospheric modes of oscillation for example the 5 minute mode and the 3 minute chromospheric mode. The 30 s driver was selected because this corresponds to a frequency below that of the atmospheric cut-off and we can use the propagation characteristics as a test of our simulations. The periods for the normal modes were determined for different values of the speed of sound (c_s) in the solar atmosphere at different heights. The periods for the resulting drivers are shown in Table (5).

$$\omega_{nm}^2 = 2\left(\frac{\pi c_s}{L}\right)^2, \tag{16}$$

where L is the box length.

With the objective to analyse and understand the nature of the frequency shifts of the excited modes, we consider a number of cases. To determine how wave energy propagation is influenced by the wave modes and frequencies, we compute the time averaged wave energy flux integrated over the

Mode	$c_s = 20$ km/s	$c_s = 31.4$ km/s
0,0	282.8	180.0
0,1	200.0	127.3
0,2	133.3	84.8
0,3	100.0	63.6

Table 2: Time periods of extended photospheric drivers for normal modes corresponding to c_s at different heights. The first mode number corresponds to the mode for the x-direction and the second number the mode for the y-direction.

Mode	Period (s)
1,1	471.4
2,2	235.7
3,3	157.1

Table 3: Time periods of extended photospheric drivers for normal modes corresponding to equal mode numbers.

Mode	30 s driver amplitude	180 s s driver amplitude	300 s s driver amplitude
0,0	343.4	348.3	350.0
0,1	217.2	220.3	221.4
0,2	153.6	155.8	156.5
0,3	117.8	119.5	120.0

Table 4: Amplitudes of extended photospheric drivers for modes with different driver periods.

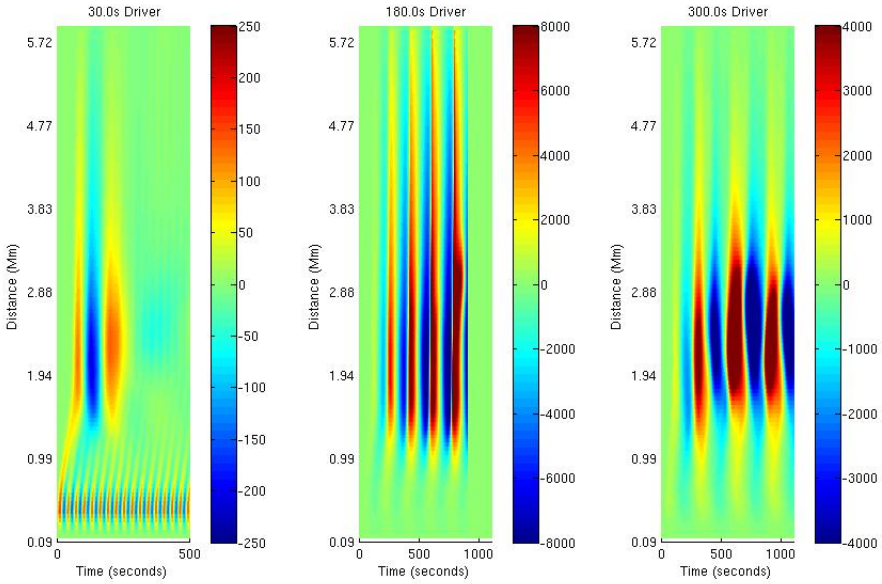

Figure 2: Time-distance plot for fundamental model and 30, 180 and 300 s driver period for the z component of the velocity for a vertical slice across the box taken at 2 Mm and shows the profile of v_z through the solar atmosphere for different time steps (the left hand plot shows the case for the 30 s driver, the centre plot the case for the 180 s driver and the right hand plot shows the case for the 300 s driver).

cross-sectional area of the simulation box at different heights. The area of integration is perpendicular to the model z axis.

$$F_{int} = \frac{1}{t_{max}} \int_0^{t_{max}} \int \mathbf{F_{wave}} \cdot d\mathbf{A}dt, \tag{17}$$

Where the wave energy flux $\mathbf{F_{wave}}$ is given by

$$\mathbf{F_{wave}} = \tilde{\mathbf{p}}_\mathbf{k}\mathbf{v} + \frac{\mathbf{1}}{\mu_\mathbf{0}}(\mathbf{B_b} \cdot \tilde{\mathbf{B}})\mathbf{v} - \frac{\mathbf{1}}{\mu_\mathbf{0}}(\mathbf{v} \cdot \tilde{\mathbf{B}})\mathbf{B_b} \tag{18}$$

The expression for the wave energy flux used by $\tilde{p}_k$ is the perturbed kinetic pressure given by Bogdan et al. (2003)

$$\tilde{p}_k = (\gamma - 1)(\tilde{e} - \frac{(\tilde{\rho} + \rho_b)\mathbf{v}^2}{2} - \frac{\tilde{\mathbf{B}}^2}{2} - \mathbf{B_b} \cdot \tilde{\mathbf{B}}). \tag{19}$$

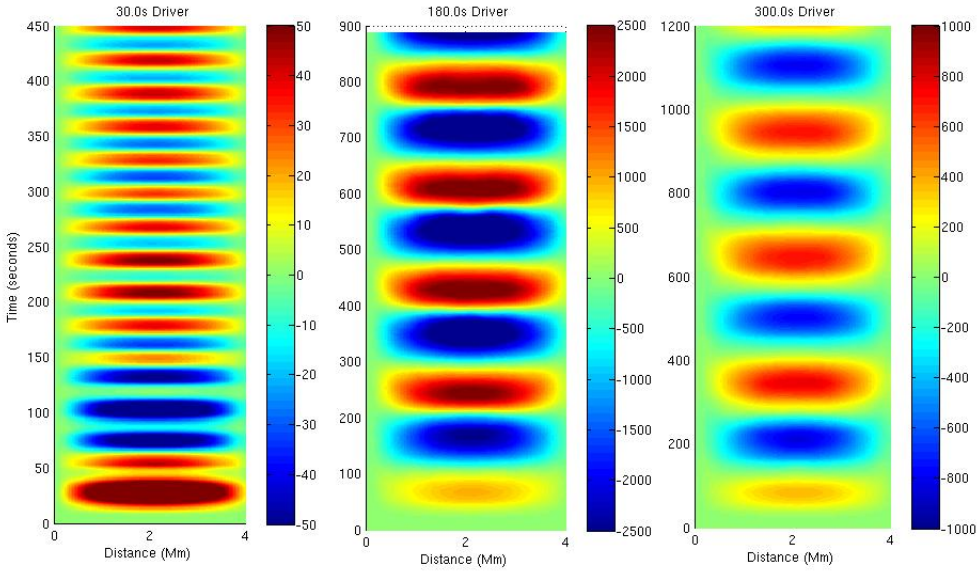

Figure 3: Time-distance plot for fundamental model $(0, 0)$ and 30, 180 and 300 s driver period for the z component of the velocity for a horizontal slice across the box taken at 0.94 Mm shows the profile of v_z across the simulation box at a given point (left hand is 30 s driver, centre is 180 s driver and the right hand is the 300 s driver).

6. Results of Numerical Simulation

The propagation of waves in a stratified atmosphere can be understood using linearised versions of the equation of continuity, momentum and energy. Such atmospheric waves of expansion have been considered for many years, initiated by e.g. Lamb (1932).

Owing to the high gradients, partial reflection of acoustic waves at all frequencies is expected at the transition region. The transition region is the upper boundary of the chromospheric cavity, it has been previously suggested that this is the source of three-minute transition-region oscillations Leibacher and Stein (1971).

It is known that the propagation of acoustic waves in an unbounded stratified medium is determined by a cut-off period. In a gravitationally stratified atmosphere acoustic waves can only propagate if the wave period is less than the cut-off period. Waves with a period greater than the cut-off are evanescent.

Following Taroyan and Erdélyi (2008), by solving the Klein-Gordon equa-

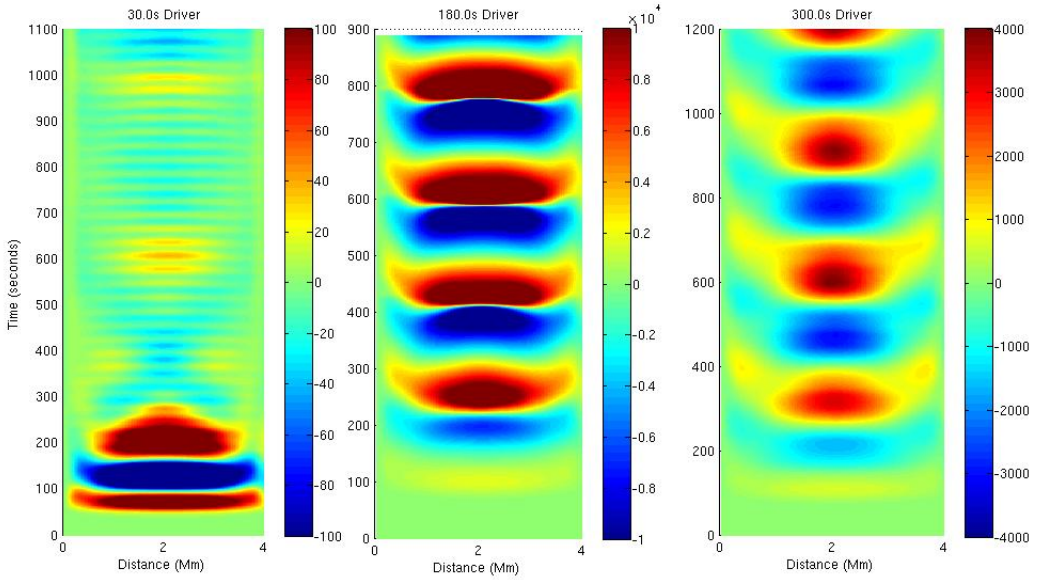

Figure 4: Time-distance plot for fundamental model and 30, 180 and 300 s driver period for the z component of the velocity for a horizontal slice across the box taken at the transition zone shows the profile of v_z across the simulation box at a height of 2 Mm (left hand is 30 s driver, centre is 180 s driver and the right hand is the 300 s driver).

tion for the gravitationally stratified atmosphere equation (20), the cut-off for the atmosphere can be obtained from equation (21)

$$\frac{\partial^2 Q}{\partial t^2} - c_s^2(z)\frac{\partial^2 Q}{\partial z^2} + \Omega^2(z)Q = 0, \tag{20}$$

$$P_c(z) = \frac{2\Lambda_0}{c_s(z)}\sqrt{\frac{1}{1 + 2\frac{d}{dz}\Lambda_0(z)}}. \tag{21}$$

The pressure scale height for an atmosphere stratified by a uniform gravitational field is given by

$$\Lambda_0(z) = \frac{p_0(z)}{g\rho_0(z)}, \tag{22}$$

Here, $p_0(z)$ and $\rho_0(z)$ are the variation of the equilibrium pressure and density with height, respectively. Q is the rescaled velocity perturbation. The variation of the cut-off frequency as a function of solar atmospheric height is shown in Figure (1) (right panel) which unveils the cut-off period

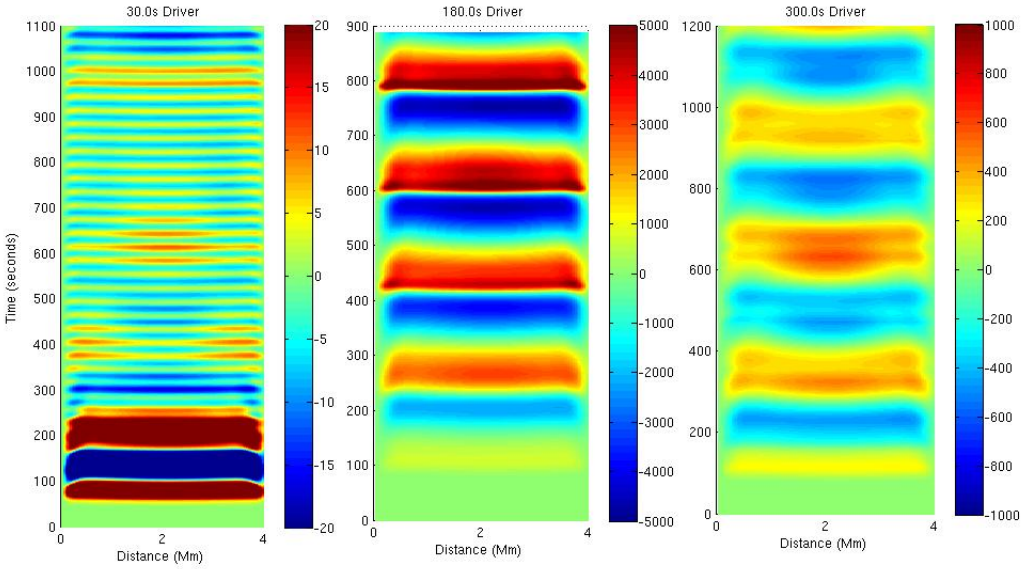

Figure 5: Time-distance plot for fundamental model and 30, 180 and 300 s driver period for the z component of the velocity for a horizontal slice across the box taken at 4.2 Mm shows the profile of v_z across the simulation box (left hand is 30 s driver, centre is 180 s driver and the right hand is the 300 s driver).

for the case of VALIIIc atmosphere and isothermal atmosphere, respectively. It is recognised from Figure (1) that there are a number of distinct regions of propagation behaviour. For the photosphere near the temperature minimum the cut-off period is 300 s, therefore it is expected that the 5 minutes modes are evanescent. In the chromosphere the cut-off period increases to a value greater than 300 s, therefore the five minute modes can propagate once they are either excited here or can propagate here due to e.g. leakage. For the transition zone the cut-off drops to a value which goes down to 100 s. In the corona, it is seen that a much greater range of frequencies can propagate.

The full set of videos for all the simulations performed have been made publically available on the digital media repository hosted by The University of Sheffield, see Griffiths et al. (2017). Each video shows the value of the vertical component of the plasma velocity (z-component) along different slices through the simulation box. The scale shows the velocity in m/s. The green vectors represent the velocity directions along a single slice through the simulation. The green surface at a height of 3.5 Mm is the 2 MK tempera-

Label	Density profile	Gravity enabled	Driver
B	VALIIC	yes	single driver at photosphere
C	VALIIC	no	single driver at photosphere
D	constant density	yes	single driver at photosphere
E	constant density	no	single driver at photosphere
F	constant density	no	two drivers at the photosphere
and transition zone			

Table 5: Simulations used to characterise oscillatory motions arising from the surface driver.

ture isosurface. Each video is labelled using 3 numbers. The first number is the driver period in seconds. The following 2 integers are each of the mode indices for the x and y direction respectively.

For the fundamental modes $(0, 0)$ illustrated in Figures (3-5) we observe that there is no significant structure at the transition zone. However, the 30 s mode demonstrates the rapid expansion of the perturbation at the penetration height of the the transition region. This is accompanied with an increase in the transverse velocity (v_x). This observation is true for all 30, 180 and 300 s driver scenarios. As the mode order is increased from $n = 0$, to $n = 1$ and then $n = 2$ its is observed that transition region structuring becomes apparent and is more reminiscent of the observations of Malins (2007).

For the fundamental modes with the 30, 180 and 300 s drivers we have plotted time-distance plots of v_z of the plasma velocity, i.e., in the same direction as the driver and in the direction of increasing height through the solar atmosphere. Figure (6) shows the time-distance plots for a vertical section through the simulation box. Since this was a fundamental mode the section was taken through the middle of the simulation box. The plots show that the greatest amplitude arises in the transition region, in particular for the 180 s driver. Looking at the result for the 30 s driver, it is seen that the initial travelling response reaches a response at around 0.5 Mm corresponding to a cut-off of 200 s. The maximum amplitude is coherent with the maximum occurring at the same frequency as that of the driver. For the first 70 periods maxima appear in the transition zone. It also appears that the transition zone is essentially a source of excitation with frequency lower than that of the driver, however, at longer time periods these motions occur with reduced amplitude but with the same period as the driver. For the180 and 300 s drivers it is observed that the amplitude in the transition

zone is larger than that for the 30 s driver by a factor of up to 20. For the 30, 180 and 300 s cases we observe the travelling wave in the chromosphere and in the solar corona. Although the 180 s mode shows the greatest excitation both the 180 and 300 s drivers become evanescent due the the cut-off period for the upper atmosphere. Figure 10 and figure 13show the time-distance plots for a horizontal section taken at a height of 0.94 Mm, i.e. through the chromosphere. The travelling modes in these plots propagate as plane modes with a frequency consistent with that of the driver. The greatest intensity is observed for the 180 s driver. Propagation for the transition zone shows the most powerful response for the 180 s driver followed by the 300 s driver. The response for the 30 s driver decays rapidly after the first ten cycles. As we move into the solar corona there is further attenuation with the greatest signal reduction for the 30 s driver.

The time-distance plots for horizontal sections at an atmospheric height of 4.2 Mm are a clear indication of the propagation of waves across the transition zone. For the case of the 30 s driver it can be seen that the propagation is cut-off after the first 270 s of the simulation. All three driver cases indicate a peak with a width of around 90 s. This peak exhibits a degree of splitting which is most clear for the 300 s driver. This effect may be attributable to the superposition of waves reflected from the boundaries of the chromosphere.

Using Equation (17), we compute the energy flux integral for the range of driver frequencies, modes and at different atmospheric heights. Figure (16) shows the variation of the energy flux ratio. We compute the ratio of the energy flux at a height of 5.5 Mm to the driver energy ratio. Figure 15 shows the energy ratios for the different modes. Fitting the data for the $(0, 0)$ mode against the power law shown in equation (23) gives the values shown in table 6. The power law values are in agreement with the values obtained from the observational results of Ireland et al. (2015) who are distinguishing a flat power spectrum for high frequencies and a power spectrum for low frequencies.

$$P(z) = aT^b + c, \tag{23}$$

The tables show the resulting values of the energy flux from the simulations at different heights. All the modes for the driver periods 180 and 300 s are shown as a bar chart in Figures (**??**) and (18). For both the 180 and 300 s drivers it can be seen that the even modes make the strongest contribution in the corona. The results plotted in Figure (19) indicate the ratio of the

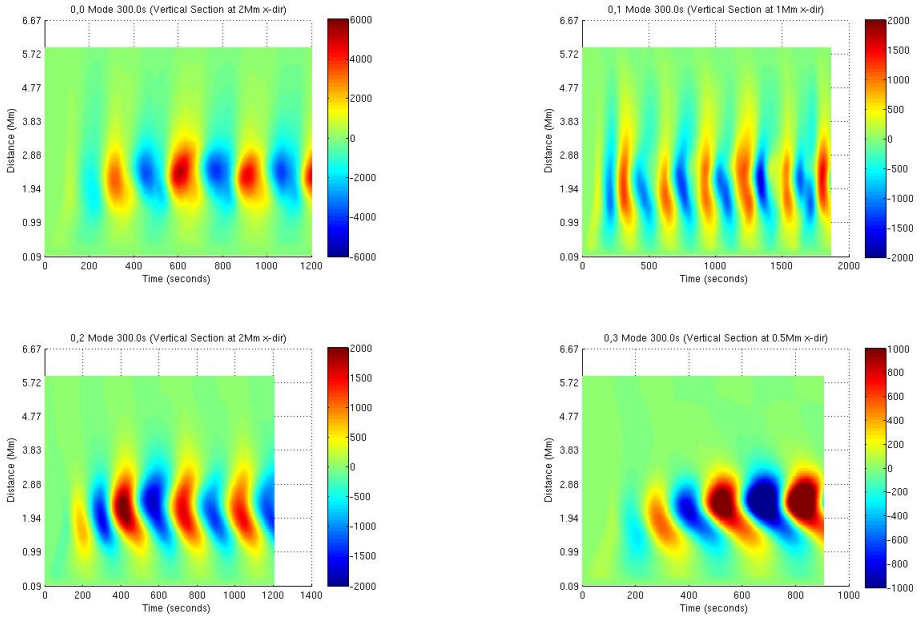

Figure 6: Time-distance plot for fundamental model with 300 s period for the z component of the velocity. x-direction

energy flux for models delivering the same quantity of energy to the energy flux for models where the driver amplitude is kept fixed. With the exception of the fundamental mode, the ratios appear to be constant for all frequencies suggesting the possibility of using the scaling relation to compute the energy flux for different frequencies and modes.

7. Conclusions

Our results support the notion that solar global oscillations are a driver for a range of global dynamical phenomena resulting in chromospheric and low coronal oscillations which may contribute to the energy in the solar atmosphere. Global dynamical phenomena arise from a range of sources including solar global oscillations, turbulent motions from convective cells and nano flares giving the possibility of continuous reconnection events.

1. The consistency of the frequency-dependence of the energy flux for our numerical simulations and power flux measurements obtained from

	Fitted Values	Ireland (171Å)	Ireland (193Å)
a	-6.199x10^{-9}	$10^{0.57}$	$10^{-0.1}$
b	1.762	1.72	2.2
c	0.002872	10^{-3}	$10^{-3.52}$

Table 6: Power law coefficients for relationship between power and time-period of atmospheric oscillation.

	1 Mm	2 Mm	4 Mm	5.5 Mm
30	0.0133	1.7275x10^{-4}	1.0561x10^{-4}	5.5399x10^{-5}
300	0.2607	0.008144	0.002176	0.001119
180	0.7227	0.047895	0.019831	0.010365
435.1	1.9415	0.043601	0.005944	0.003147
179.98	1.6450	0.004502	0.002600	0.001366
282.84	0.1986	0.004007	0.001845	9.7821x10^{-4}

Table 7: $(0, 0)$ mode energy ratio.

	1 Mm	2 Mm	4 Mm	5.5 Mm
30	0.0065	1.751x10^{-5}	1.2579x10^{-6}	4.6820x10^{-7}
300	0.1001	8.796x10^{-4}	4.1494x10^{-6}	1.3059x10^{-6}
180	0.1543	5.8381x10^{-4}	3.2715x10^{-5}	1.1343 x10^{-5}
307.1	0.0982	0.001	4.1351x10^{-6}	1.3380 x10^{-6}
127.27	0.0829	4.3190x10^{-4}	5.1387x10^{-5}	2.0397 x10^{-5}
200.0	0.1126	4.4180x10^{-4}	2.0186x10^{-5}	6.3062 x10^{-6}

Table 8: $(0, 1)$ mode energy ratio.

	1 Mm	2 Mm	4 Mm	5.5 Mm
30	0.0024	7.2158 x10^{-6}	1.0651x10^{-6}	7.6079x10^{-7}
300	0.0578	4.9604 x10^{-4}	5.5618x10^{-6}	4.1907x10^{-6}
180	0.0687	3.5547 x10^{-4}	6.0675x10^{-5}	4.1492 x10^{-5}
205.1	0.3135	0.0015	1.6520x10^{-4}	1.1272x10^{-4}
84.84	0.0206	5.8903 x10^{-5}1.6520 x10^{-5}	1.1890 x10^{-5}	
133.33	0.0497	1.9731x10^{-4}7.9834 x10^{-5}	5.6267 x10^{-5}	

Table 9: $(0, 2)$ mode energy ratio.

	1 Mm	2 Mm	4 Mm	5.5 Mm
30	0.0101	$4.2736\text{x}10^{-5}$	$6.3291\text{x}10^{-7}$	$3.7786\text{x}10^{-7}$
300	0.0359	$3.8929\text{x}10^{-4}$	$3.2621\text{x}10^{-7}$	$2.1259\text{x}10^{-7}$
180	0.0351	$1.3948\text{x}10^{-4}$	$3.1342\text{x}10^{-6}$	$1.8205\text{x}10^{-6}$
153.8	0.0313	$1.1043\text{x}10^{-4}$	$3.8071\text{x}10^{-6}$	$2.1034\text{x}10^{-6}$
63.63	0.0051	$9.8989\text{x}10^{-6}$	$7.0207\text{x}10^{-7}$	$4.0621\text{x}10^{-7}$
100.0	0.0151	$3.0678\text{x}10^{-5}$	$2.8527\text{x}10^{-6}$	$1.6707\text{x}10^{-6}$

Table 10: $(0, 3)$ mode energy ratio.

	1 Mm	2 Mm	4 Mm	5.5 Mm
$(0, 0)$	0.7227	0.0479	0.0198	0.0104
$(0, 1)$	0.1543	0.0006	$3.2715\text{x}10^{-5}$	$1.1343\text{x}10^{-5}$
$(0, 2)$	0.0687	0.0004	$6.0675\text{x}10^{-5}$	$4.1492\text{x}10^{-5}$
$(0, 3)$	0.0351	0.0001	$3.1342\text{x}10^{-6}$	$1.8205\ \text{x}10^{-6}$
$(1, 1)$	0.4072	0.0011	$4.5311\text{x}10^{-6}$	$5.5495\text{x}10^{-7}$
$(1, 2)$	0.3331	0.0012	$3.0728\text{x}10^{-6}$	$1.3055\text{x}10^{-6}$
$(1, 3)$	0.2961	0.0011	$4.8733\text{x}10^{-7}$	$3.4760\text{x}10^{-7}$
$(2, 2)$	0.3054	0.0011	$1.5844\text{x}10^{-5}$	$1.7622\text{x}10^{-5}$
$(2, 3)$	0.2732	0.0008	$2.1443\text{x}10^{-6}$	$1.7045\text{x}10^{-6}$
$(3, 3)$	0.2205	0.0006	$1.9711\text{x}10^{-7}$	$2.6756\text{x}10^{-7}$

Table 11: 180 s driver energy ratio.

	1 Mm	2 Mm	4 Mm	5.5 Mm
$(0, 0)$	0.2607	0.0081	$2.2\text{x}10^{-3}$	$1.1\text{x}10^{-3}$
$(0, 1)$	0.1001	0.0009	$4.1494\text{x}10^{-6}$	$1.3059\text{x}10^{-6}$
$(0, 2)$	0.0578	0.0005	$5.5618\text{x}10^{-6}$	$4.1907\text{x}10^{-6}$
$(0, 3)$	0.0359	0.0004	$3.2621\text{x}10^{-7}$	$2.1259\text{x}10^{-7}$
$(1, 1)$	0.2267	0.0016	$9.9329\text{x}10^{-7}$	$1.0749\text{x}10^{-7}$
$(1, 2)$	0.2535	0.0016	$8.2058\text{x}10^{-7}$	$2.8814\text{x}10^{-7}$
$(1, 3)$	0.2692	0.0023	$2.1995\text{x}10^{-7}$	$9.0161\text{x}10^{-8}$
$(2, 2)$	0.2625	0.0021	$1.4846\text{x}10^{-6}$	$1.7399\text{x}10^{-6}$
$(2, 3)$	0.2328	0.0017	$2.4839\text{x}10^{-7}$	$2.0699\text{x}10^{-7}$
$(3, 3)$	0.2036	0.0012	$7.2069\text{x}10^{-8}$	$4.944\text{x}10^{-8}$

Table 12: 300 s driver energy ratio percentage.

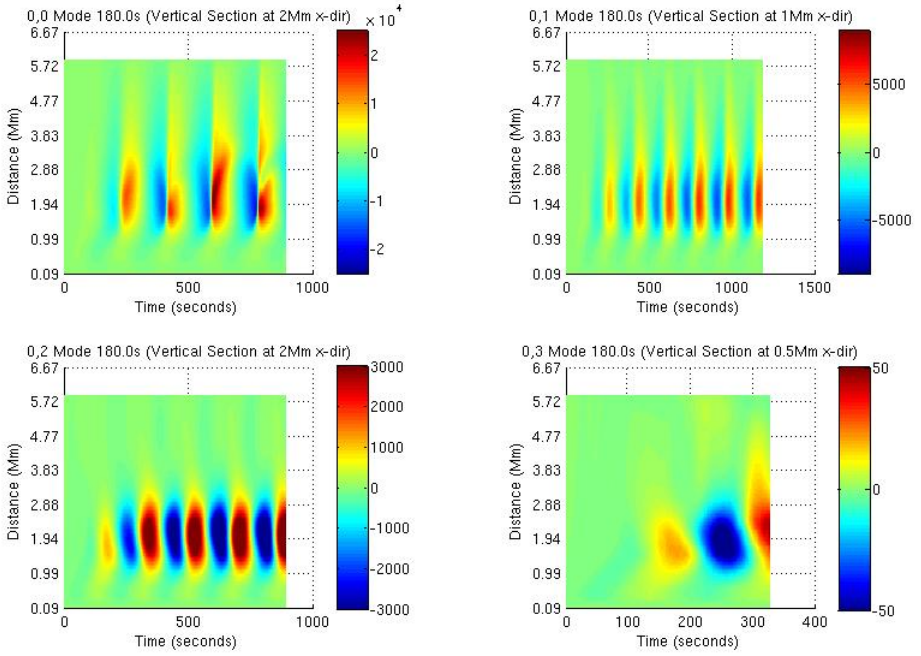

Figure 7: Time-distance plot for fundamental model with 180 s period for the z component of the velocity. x-direction

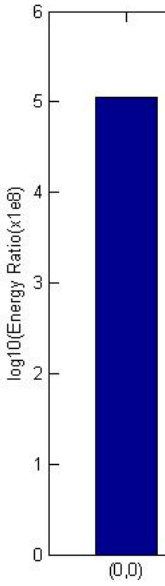

Figure 18: Variation of e
with a 300 s p-mode dri

SDO motivates the use of numerical simulations for modelling the excitations driven by solar global oscillations for the quiet sun.

2. Energy propagation into the mid to upper atmosphere occurs for a range of frequencies and may explain observed intensity oscillations for periods greater than the well known 3 minute and 5 minute oscillations.
3. Energy flux propagation into the solar corona is strongly dependent on the wave modes.
4. Agreement between the energy flux predictions of our numerical simulations and the the two layer Klein-Gordon model supports our interpretation of the interaction of solar global oscillations with the solar atmosphere.

8. Acknowledgements

RE acknowledges M. Kéray for patient encouragement and is also grateful to NSF, Hungary (OTKA, Ref. No. K83133). The authors thank the

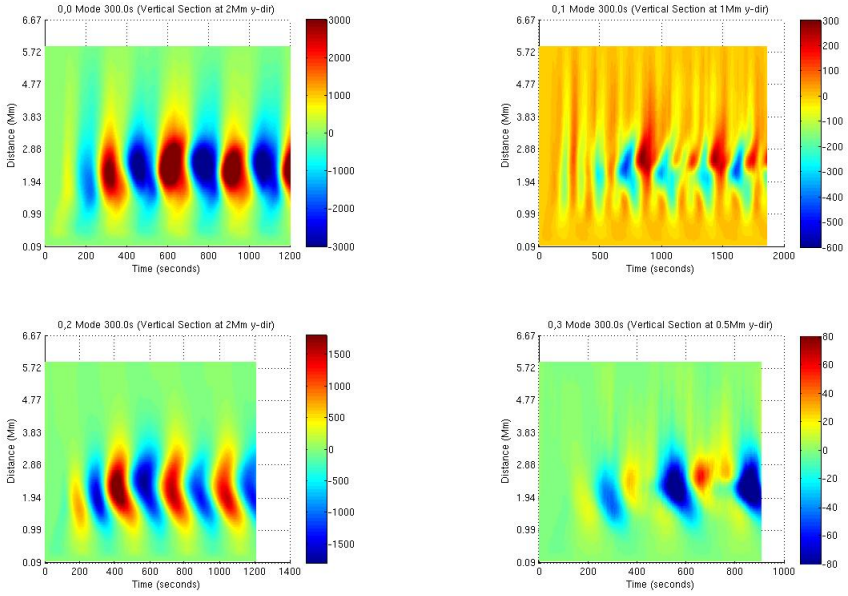

Figure 8: Time-distance plot for fundamental model with 300 s period for the z component of the velocity. y-direction

Science and Technology Facilities Council (STFC), UK for the support they received. VF thanks the Royal Society-Newton Mobility Grant and Newton Fund MAS/CONACyT Mobility Grants Program for the support received. We acknowledge Corporate Information and Computing Services at The University of Sheffield for the provision of the High Performance Computing Service.

References

References

Beck, C., Rezaei, R., Puschmann, K. G., Aug. 2012. The energy of waves in the photosphere and lower chromosphere. II. Intensity statistics. A&A544, A46.

Bello González, N., Flores Soriano, M., Kneer, F., Okunev, O., Dec. 2009. Acoustic waves in the solar atmosphere at high spatial resolution. A&A508, 941–950.

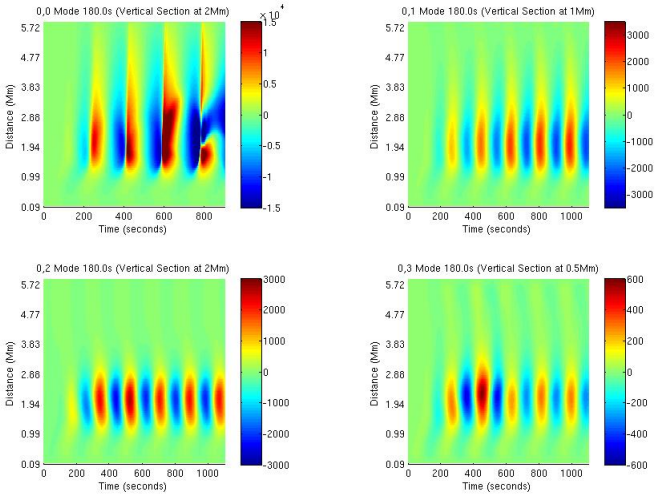

Figure 9: Time-distance plot for fundamental model with 180 s period for the z component of the velocity. y-direction

Bello González, N., Flores Soriano, M., Kneer, F., Okunev, O., Shchukina, N., Nov. 2010. Acoustic waves in the solar atmosphere at high spatial resolution. II. Measurement in the Fe I 5434 Å line. A&A522, A31.

Bogdan, T. J., Carlsson, M., Hansteen, V. H., McMurry, A., Rosenthal, C. S., Johnson, M., Petty-Powell, S., Zita, E. J., Stein, R. F., McIntosh, S. W., Nordlund, Å., Dec. 2003. Waves in the Magnetized Solar Atmosphere. II. Waves from Localized Sources in Magnetic Flux Concentrations. ApJ599, 626–660.

Brown, T. M., Stebbins, R. T., Hill, H. A., 1978. Long-period oscillations of the apparent solar diameter - Observations. ApJ223, 324–338.

Carlsson, M., Stein, R. F., 1995. Does a nonmagnetic solar chromosphere exist? ApJL440, L29–L32.

Caunt, S. E., Korpi, M. J., Apr. 2001. A 3D MHD model of astrophysical flows: Algorithms, tests and parallelisation. A&A369, 706–728.

De Moortel, I., Dec. 2005. An overview of coronal seismology. Philosophical Transactions of the Royal Society of London Series A 363, 2743–2760.

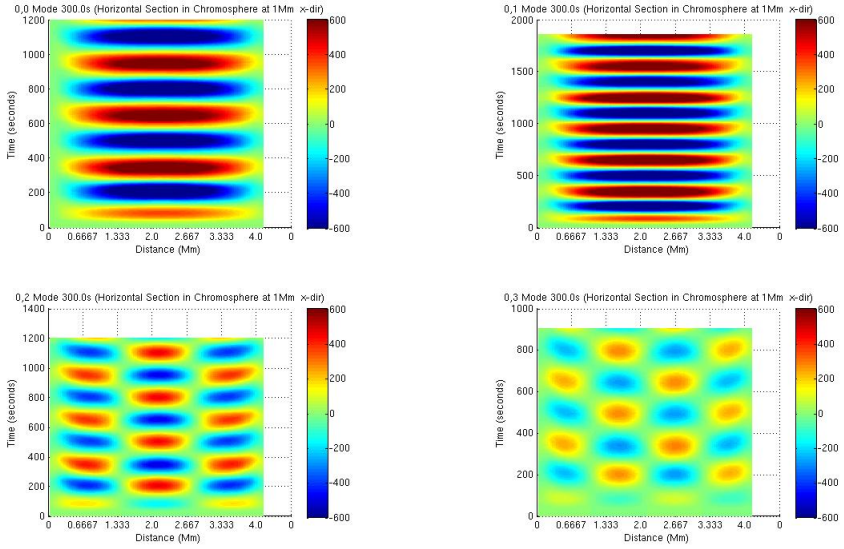

Figure 10: Time-distance plot for modes with 300 s period horizontal section through the chromosphere (at 1 Mm) for the z component of the velocity. x-direction

Erdélyi, R., Zheng, R., Verth, G., Keys, P., submitted 2017. Ubiquitous concurrent intensity oscillations in the solar atmosphere detected by SDO/AIA. ApJ, 25.

Fedun, V., Erdélyi, R., Shelyag, S., Sep. 2009. Oscillatory Response of the 3D Solar Atmosphere to the Leakage of Photospheric Motion. Sol. Phys.258, 219–241.

Goedbloed, J., Poedts, S., 2004. Principles of Magnetohydrodynamics: With Applications to Laboratory and Astrophysical Plasmas. Cambridge University Press.
URL https://books.google.co.uk/books?id=FvM6rMJob-cC

Griffiths, M., Erdélyi, R., Fedun, V., 4 2017. Videos of Magnetohydrodynamics Simulations of Solar Atmosphere Wave Dynamics Generated by Solar Global Oscillating Eigenmodes.
URL https://figshare.com/articles/Videos_of_Magnetohydrodynamics_Simulations_of_Solar_Atmosphere_Wave_

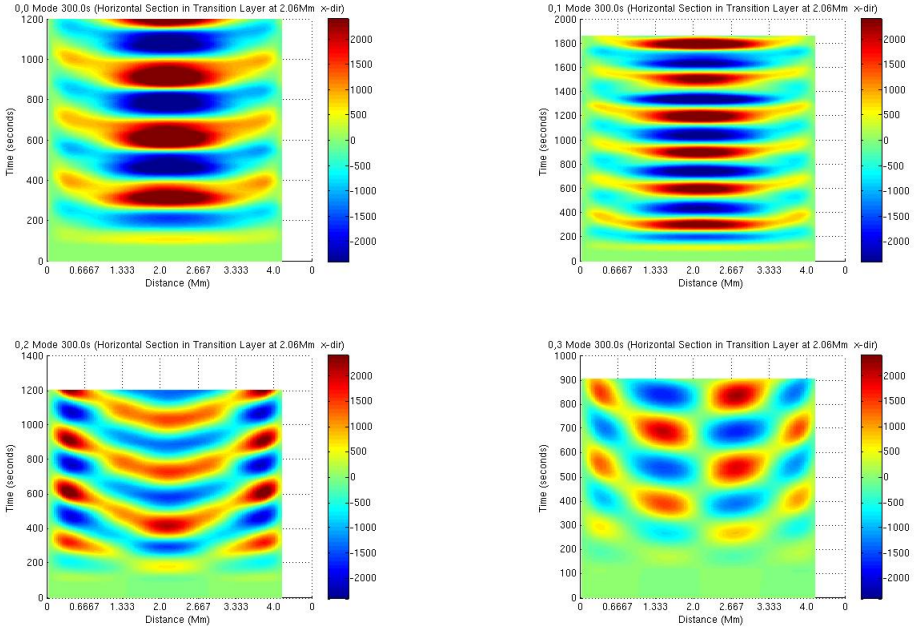

Figure 11: Time-distance plot for modes with 300 s period, horizontal section through the Transition Region (at 2.06 Mm) for the z component of the velocity. x-direction

Dynamics_Generated_by_Solar_Global_Oscillating_Eigenmodes/4818490

Griffiths, M. K., Fedun, V., Erdélyi, R., 2015. A Fast MHD Code for Gravitationally Stratified Media using Graphical Processing Units: SMAUG. Journal of Astrophysics and Astronomy 36, 197–223.

Hill, H. A., 1976. Talk on Solar Diameter Oscillations. The Observatory 96, 130–132.

Ireland, J., McAteer, R. T. J., Inglis, A. R., 2015. Coronal Fourier Power Spectra: Implications for Coronal Seismology and Coronal Heating. ApJ798, 1.

Jefferies, S. M., McIntosh, S. W., Armstrong, J. D., Bogdan, T. J., Cacciani, A., Fleck, B., Oct. 2006. Low-frequency magneto-acoustic waves in the solar chromosphere. In: Proceedings of SOHO 18/GONG

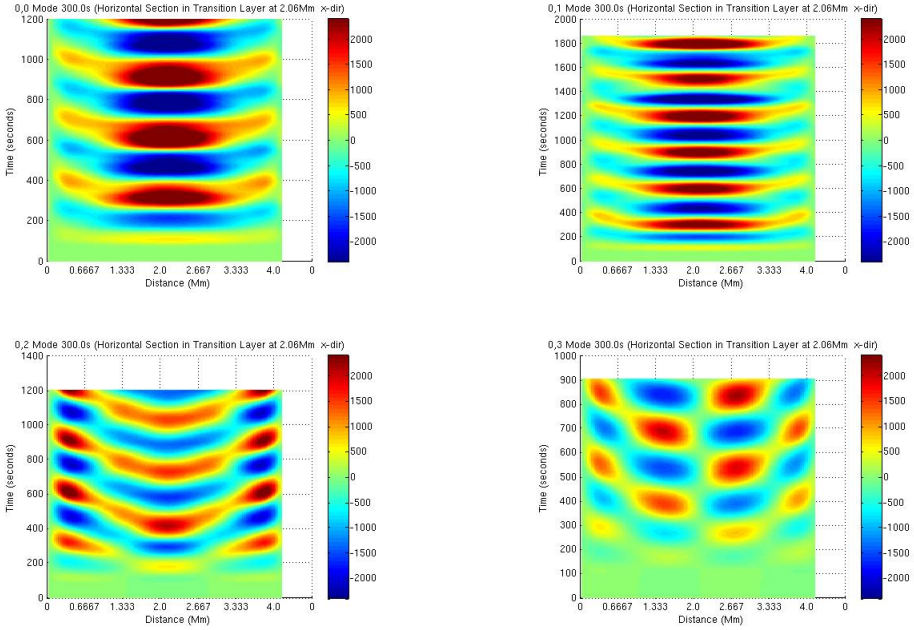

Figure 12: Time-distance plot for modes with 300 s period Horizontal Section through the Solar Corona (at 4.3 Mm) for the z component of the velocity. x-direction

2006/HELAS I, Beyond the spherical Sun. Vol. 624 of ESA Special Publication. p. 16.1.

Kalkofen, W., 2012. The Validity of Dynamical Models of the Solar Atmosphere. Sol. Phys.276, 75–95.

Kalkofen, W., Rossi, P., Bodo, G., Massaglia, S., Sep. 2010. Acoustic waves in a stratified atmosphere. IV. Three-dimensional nonlinear hydrodynamics. A&A520, A100.

Khomenko, E., Calvo Santamaria, I., Jun. 2013. Magnetohydrodynamic waves driven by p-modes. Journal of Physics Conference Series 440 (1), 012048.

Lamb, H., 1932. Hydrodynamics.

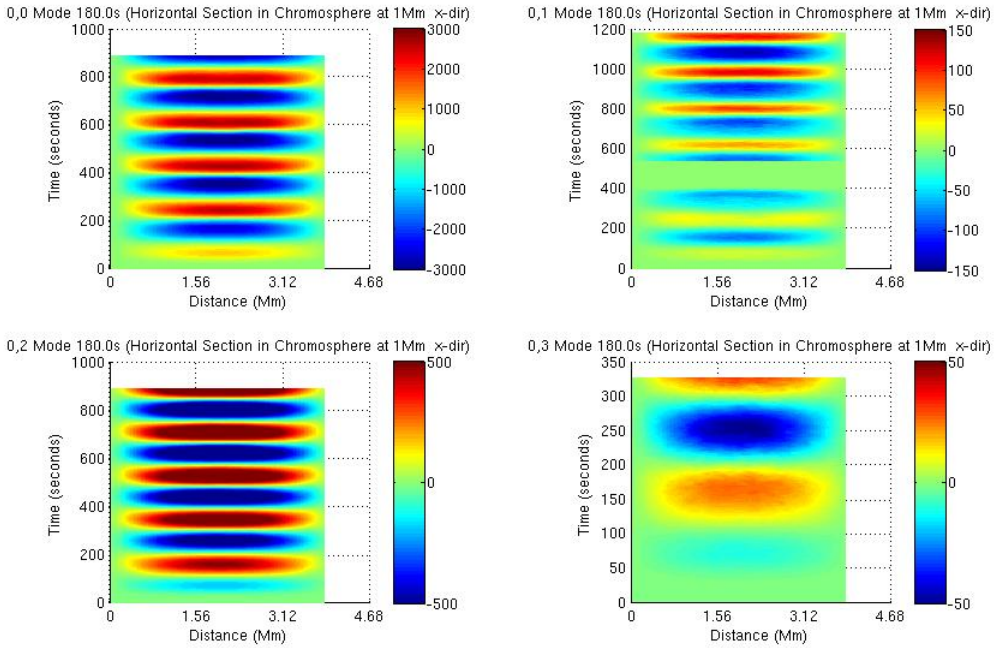

Figure 13: Time-distance plot for modes with 180 s period Horizontal Section through the Chromosphere (at 1 Mm) for the z component of the velocity. x-direction

Leenaarts, J., Carlsson, M., Hansteen, V., Gudiksen, B. V., 2011. On the minimum temperature of the quiet solar chromosphere. A&A530, A124.

Leibacher, J. W., Stein, R. F., 1971. A New Description of the Solar Five-Minute Oscillation. 7, 191–192.

Leighton, R. B., 1960. In: Thomas, R. N. (Ed.), Aerodynamic Phenomena in Stellar Atmospheres. Vol. 12 of IAU Symposium. pp. 321–325.

Lites, B. W., Kubo, M., Socas-Navarro, H., Berger, T., Frank, Z., Shine, R., Tarbell, T., Title, A., Ichimoto, K., Katsukawa, Y., Tsuneta, S., Suematsu, Y., Shimizu, T., Nagata, S., Jan. 2008. The Horizontal Magnetic Flux of the Quiet-Sun Internetwork as Observed with the Hinode Spectro-Polarimeter. ApJ672, 1237–1253.

Malins, C., 2007. On transition region convection cells in simulations of {p}-mode propagation. Astronomische Nachrichten 328, 752–755.

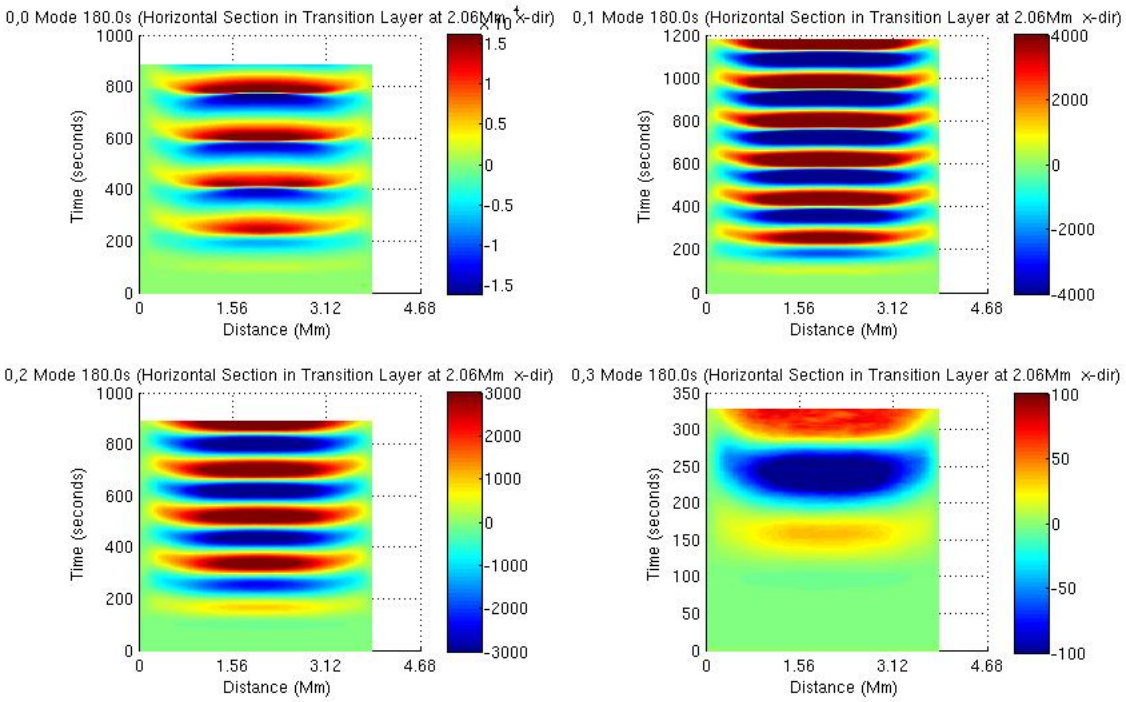

Figure 14: Time-distance plot for modes with 180 s period Horizontal Section through the Transition Region (at 2.06 Mm) for the z component of the velocity. x-direction

McWhirter, R. W. P., Thonemann, P. C., Wilson, R., 1975. The heating of the solar corona. II - A model based on energy balance. A&A40, 63–73.

Murawski, K., Zaqarashvili, T. V., Sep. 2010. Numerical simulations of spicule formation in the solar atmosphere. A&A519, 9.

Roberts, B., Edwin, P. M., Benz, A. O., Apr. 1984. On coronal oscillations. ApJ279, 857–865.

Roth, M., Franz, M., Bello González, N., Martínez Pillet, V., Bonet, J. A., Gandorfer, A., Barthol, P., Solanki, S. K., Berkefeld, T., Schmidt, W., del Toro Iniesta, J. C., Domingo, V., Knölker, M., 2010. Surface Waves in Solar Granulation Observed with SUNRISE. ApJL723, L175–L179.

Shelyag, S., Fedun, V., Erdélyi, R., Aug. 2008. Magnetohydrodynamic code for gravitationally-stratified media. A&A486, 655–662.

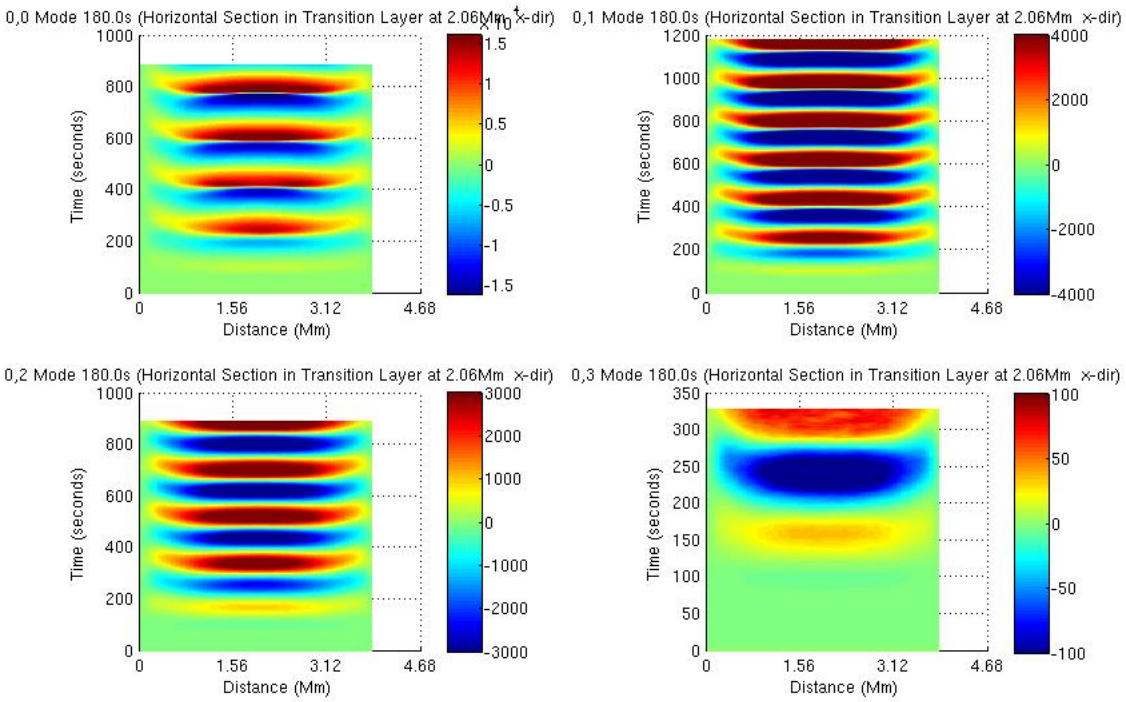

Figure 15: Time-distance plot for modes with 180 s period Horizontal Section through the Solar Corona (at 4.3 Mm) for the z component of the velocity. x-direction

Taroyan, Y., Erdélyi, R., 2008. Global Acoustic Resonance in a Stratified Solar Atmosphere. Sol. Phys.251, 523–531.

Tóth, G., 1996. A General Code for Modeling MHD Flows on Parallel Computers: Versatile Advection Code. Astrophysical Letters and Communications 34, 245.

Ulrich, R. K., Dec. 1970. The Five-Minute Oscillations on the Solar Surface. ApJ162, 993.

Vernazza, J. E., Avrett, E. H., Loeser, R., Apr. 1981. Structure of the solar chromosphere. III - Models of the EUV brightness components of the quiet-sun. 45, 635–725.

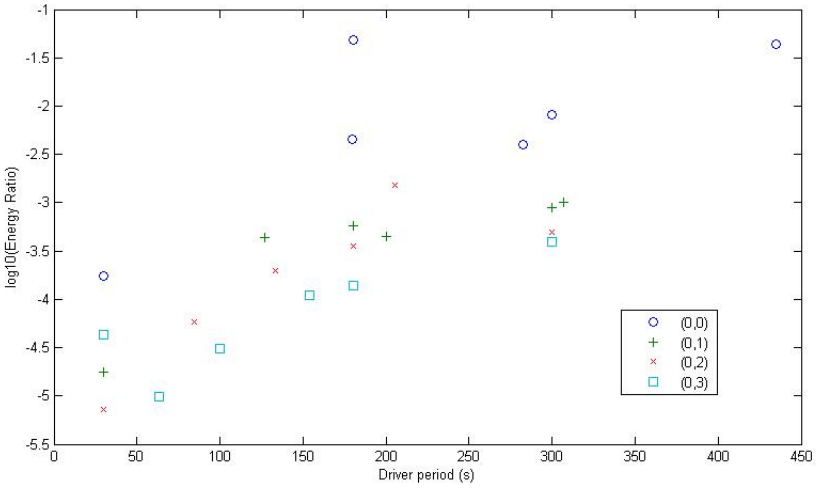

Figure 16: Variation of energy flux ratio with the driver energy at height of 5.5 Mm for a solar atmosphere excited with a $itp - modedriverlocatedataheightof50km$

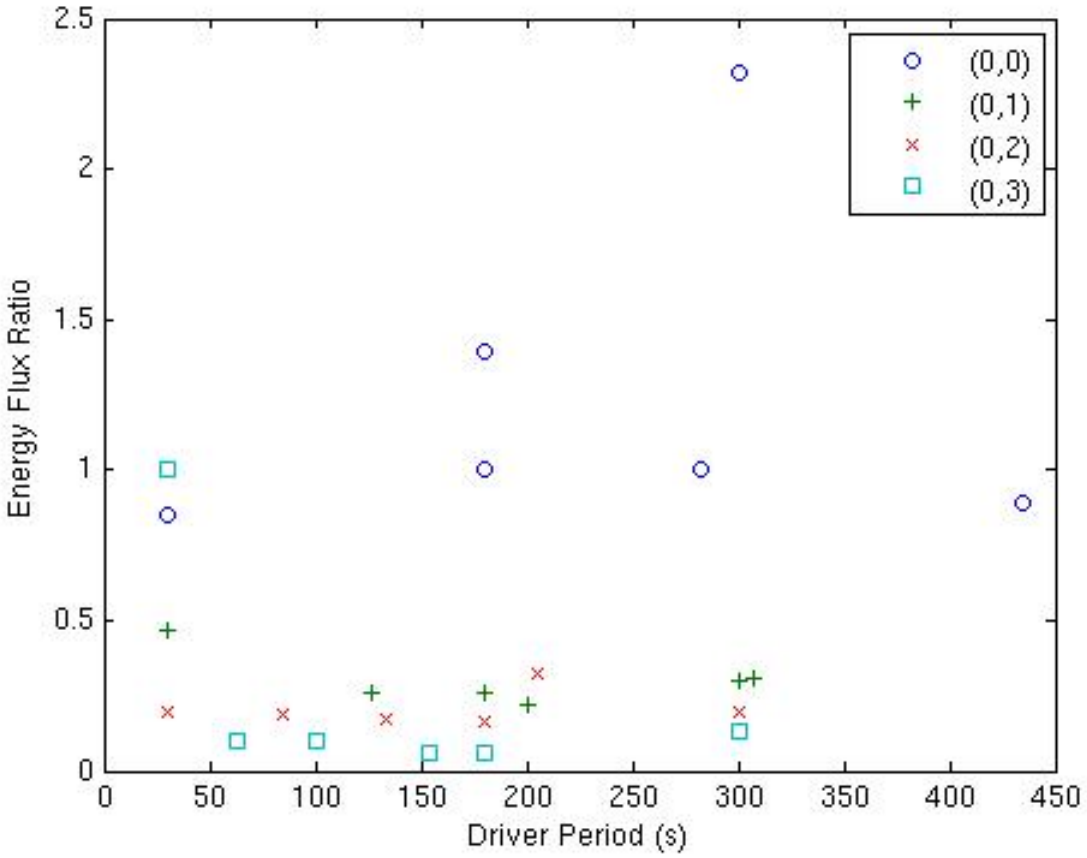

Figure 19: Variation of energy flux ratio at height of 5.5 Mm for a solar atmosphere excited with a p-mode driver located at height of 50 km